2-21-2018

Spectrally based bathymetric mapping of a dynamic, sandbedded channel: Niobrara River, Nebraska, USA

E. Dilbone

C.J. Legleiter

J.S. Alexander

B. McElroy

Received: 27 July 2017 | Revised: 10 January 2018 | Accepted: 21 February 2018

DOI: 10.1002/rra.3270

RESEARCH ARTICLE

WILEY

Spectrally based bathymetric mapping of a dynamic, sand-bedded channel: Niobrara River, Nebraska, USA

E. Dilbone[1] | C.J. Legleiter[1,2] | J.S. Alexander[3] | B. McElroy[3]

[1]Department of Geography, University of Wyoming, Laramie, Wyoming, USA

[2]U.S. Geological Survey, Geomorphology and Sediment Transport Laboratory, Golden, Colorado, USA

[3]Department of Geology and Geophysics, University of Wyoming, Laramie, Wyoming, USA

Correspondence
C. J. Legleiter, U.S. Geological Survey, Geomorphology and Sediment Transport Laboratory, 4620 Technology Drive, Suite #400, Golden, CO 80403, USA.
Email: cjl@usgs.gov; cleglei1@uwyo.edu

Funding information
Office of Naval Research, Grant/Award Number: N000141010873; Geological Society of America, Grant/Award Number: Graduate student research grants

Abstract

Methods for spectrally based mapping of river bathymetry have been developed and tested in clear-flowing, gravel-bed channels, with limited application to turbid, sand-bed rivers. This study used hyperspectral images and field surveys from the dynamic, sandy Niobrara River to evaluate three depth retrieval methods. The first regression-based approach, optimal band ratio analysis (OBRA), paired *in situ* depth measurements with image pixel values to estimate depth. The second approach used ground-based field spectra to calibrate an OBRA relationship. The third technique, image-to-depth quantile transformation (IDQT), estimated depth by linking the cumulative distribution function (CDF) of depth to the CDF of an image-derived variable. OBRA yielded the lowest depth retrieval mean error (0.005 m) and highest observed versus predicted R^2 (0.817). Although misalignment between field and image data did not compromise the performance of OBRA in this study, poor georeferencing could limit regression-based approaches such as OBRA in dynamic, sand-bedded rivers. Field spectroscopy-based depth maps exhibited a mean error with a slight shallow bias (0.068 m) but provided reliable estimates for most of the study reach. IDQT had a strong deep bias but provided informative relative depth maps. Overprediction of depth by IDQT highlights the need for an unbiased sampling strategy to define the depth CDF. Although each of the techniques we tested demonstrated potential to provide accurate depth estimates in sand-bed rivers, each method also was subject to certain constraints and limitations.

KEYWORDS

bathymetry, depth retrieval, hyperspectral, remote sensing, sand-bed river

1 | INTRODUCTION

Because depth exerts an important control on flow patterns, sediment transport, and in-stream habitat, bathymetric information is useful for numerous applications, such as habitat mapping (e.g., McKean, Isaak, & Wright, 2008; Tamminga, Hugenholtz, Eaton, & Lapointe, 2014). Identifying morphological units can also help predict where contaminants might accumulate (Marcus, Legleiter, Aspinall, Boardman, & Crabtree, 2003). In a geomorphic context, depth mapping enables study of bed configurations, bar patterns, and sediment transport. Repeat bathymetric surveys can be used to identify patterns of erosion and deposition, construct morphological sediment budgets, and infer bed material transport rates (e.g., Gaeuman, Schmidt, & Wilcock, 2003). Morphological budgets can help inform resource management by providing insight on impacts of natural and anthropogenic disturbances, such as floods and bed material extraction (e.g., Fuller & Basher, 2013).

Remote sensing of river channel geometry and fluvial processes has advanced from exploratory case studies (e.g., Lane, Westaway, & Hicks, 2003; Lejot et al., 2007; Winterbottom & Gilvear, 1997) to mature methodologies suitable for addressing applied management questions (e.g., Carbonneau, Fonstad, Marcus, & Dugdale, 2011; Whited, Kimball, Lorang, & Stanford, 2013). Advantages of remote sensing over conventional field surveys include the potential to quantify river morphology with high resolution over larger areas, longer time periods, and with greater frequency than conventional field methods (Marcus & Fonstad, 2008). In the context of live-bed, sandy rivers, aerial imaging provides

instantaneous snapshots of a transient channel morphology that cannot be characterized accurately or efficiently by much slower ground-based surveys. Remote sensing thus is uniquely capable of capturing spatial distributions of depth over timescales much shorter than the timescale of bed deformation in complex (i.e., intricate, multi-scalar), dynamic (i.e., rapidly evolving) sand-bed rivers. Further developing this capability would benefit river managers, particularly in the vast Great Plains region of the Central United States, where wide, shallow, unstable sand-bed rivers are the predominant channel type.

The river characteristic most readily derived from passive optical images is water depth. Numerous studies have demonstrated the ability to infer depth but most have focused on clear-flowing, shallow, gravel-bed rivers (Legleiter, Roberts, & Lawrence, 2009). The higher turbidity of sand-bedded rivers complicates depth retrieval by increasing light scattering within the water column, which diminishes the contribution of bottom-reflected radiance to the total radiance signal. A study on the Platte River in Nebraska using both field spectroscopy and radiative transfer modelling to test the feasibility of depth retrieval under turbid conditions found that depth estimates in such environments might be limited to shallow water (<0.5 m) and are subject to greater uncertainty (Legleiter, Kinzel, & Overstreet, 2011). To more fully realize the potential for remote sensing to support river science, depth retrieval techniques must be extended to sandy channels. The mobility of the bed in these rivers implies that the bathymetry is a moving target most effectively captured by a synoptic, instantaneous imaging approach.

Such applications motivated our assessment of image-based bathymetric mapping techniques for sand-bed rivers. The objective of this study is to test various depth retrieval methods in a complex, dynamic, sediment-laden channel, the Niobrara River, and thus identify the most suitable approach for sand-bed rivers. This analysis will help to expand the range of conditions where remote sensing might facilitate river research and management.

2 | STUDY AREA AND METHODS

2.1 | Study area and images

The Niobrara River is a large tributary to the Missouri River, draining a rural basin of approximately 35,000 km^2, mostly in northern Nebraska and dominated by agriculture and ranching (Alexander, Zelt, & Schaepe, 2009). The Niobrara gains substantial base flow as seepage from the High Plains aquifer, and much of the basin is undammed; despite some hydrologic alteration, the Niobrara maintains a relatively natural flow regime. The mean annual flow at the nearest U.S. Geological Survey gaging station (#06461500) since 1964, when a tributary was dammed, is 21 m^3/s (Alexander et al., 2009) with a 1.5-year recurrence interval flow of 52 m^3/s (Schaepe, Alexander, & Folz-Donahue, 2016). The river occasionally flows over bedrock, but bed material is dominated by sand originating from the surrounding Nebraska Sandhills and breakdown of the Cenozoic sedimentary bedrock underlying much of the basin (Alexander, Zelt, & Schaepe, 2010). Median bed material grain size for samples collected at four locations along the Niobrara ranged from 0.1 to 0.69 mm (Alexander et al., 2010).

This study focused on a 27-km segment of the Niobrara National Scenic River beginning approximately 30 km east of Valentine, Nebraska (Figure 1). The segment has a complex, dynamic sand-bed braided channel, dominated by actively migrating sandbars under most flow conditions (Alexander et al., 2010). Mean active channel width in the study area is approximately 160 m (Schaepe et al., 2016), but up to half of this width can be exposed as sand bars during base-flow conditions. The active flood plain in the study area has two primary levels: a higher level consisting of riparian woodlands dominated by cottonwood (*Populus* spp.), willow (*Salix* spp.), and dogwood (*Prunus* spp.) and a lower level consisting of shrublands dominated by sandbar willow (*Salix exgua*), indigo (*Amorpha* spp.), and bluegrass (*Cornus* spp.; Alexander et al., 2010; Johnsgard, 2007).

The Niobrara presents several management challenges. This riverine ecosystem provides high-quality habitat for turtles, fish, and three federally listed bird species. Canoeing and tubing are popular, and recreation is an important source of revenue to the local economy (Johnsgard, 2007). However, the Niobrara's substantial base flow also makes the river a valuable source of irrigation water during the late summer dry season (Alexander et al., 2009). Balancing protections of the physical, ecological, and recreational qualities of the Niobrara with agricultural interests requires a robust means of characterizing channel morphology and riverine habitat.

Hyperspectral images of the Niobrara River study reach were acquired under base-flow conditions using a Compact Airborne Spectrographic Imager (CASI) 1500H manufactured by ITRES and deployed from a manned, fixed-wing aircraft. Image data were collected on November 8, 2012, August 15, 2016, and August 18, 2016, by ITRES under clear sky conditions as a series of parallel, along-channel flight strips that required approximately 2 hr, centred on local solar noon, to complete (Legleiter, 2017). Flight plans were designed to minimize sun glint from the water surface and shadows from adjacent banks and riparian vegetation. Sensor configurations are summarized in Table 1, along with flow conditions and turbidity values measured during each flight. All image and field data sets used in this study are available through a series of data releases accessible via the U.S. Geological Survey ScienceBase Catalogue (Legleiter, 2017; Legleiter & Kinzel, 2017; Legleiter, Kinzel, Alexander, & Dilbone, 2017).

2.1.1 | Image preprocessing

ITRES radiometrically calibrated the CASI images to convert raw digital counts to spectral radiance. The images also were georeferenced by ITRES using global positioning system (GPS) and inertial motion data collected on-board the aircraft. The final deliverable from ITRES thus consisted of georeferenced radiance images, and we conducted all subsequent analyses using the MATLAB and ENVI software packages. Initial alignment of the 2012 image with field data was poor, with an offset of approximately 10 m evident as image seams. To correct this error, we iteratively adjusted parameters describing the sensor's mounting geometry until alignment between imagery and field data improved. For the August 18, 2016, image, a smaller 3-m misalignment was observed. To improve alignment for this image, we shifted the field data points relative to the image to minimize the number of observations located outside the channel as depicted on the image.

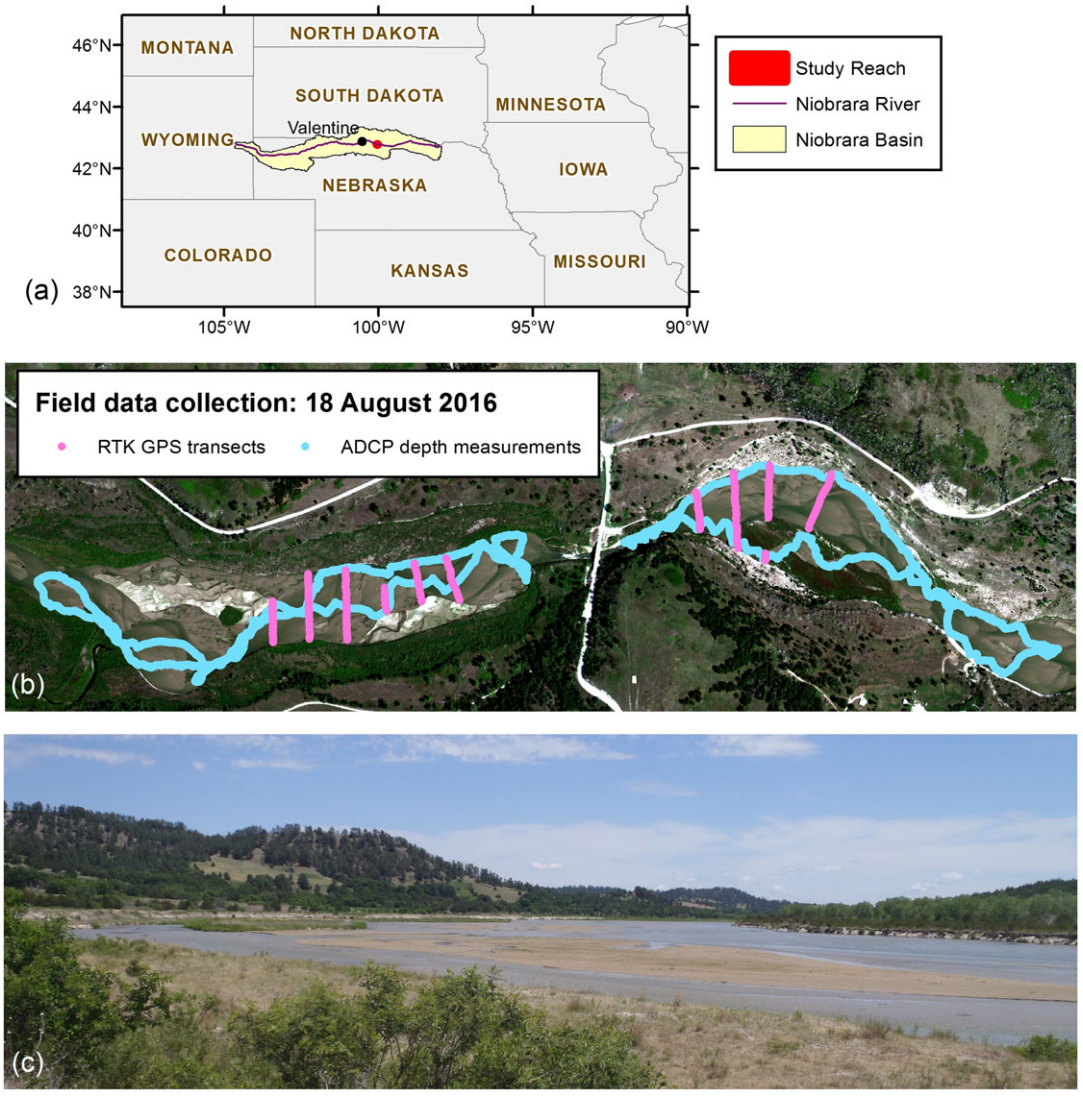

FIGURE 1 (a) Location of the Niobrara River study site in north central Nebraska, USA. (b) Subset of the August 18, 2016, Compact Airborne Spectrographic Imager (CASI) image with field measurements collected on that day. Flow direction is from left to right. (c) Ground photograph looking downstream from the county road bridge in the middle of the study area. ADCP = acoustic Doppler current profiler; GPS = global positioning system; RTK = real-time kinematic [Colour figure can be viewed at wileyonlinelibrary.com]

TABLE 1 CASI 1500 sensor characteristics, image attributes, and flow and turbidity for 2012 and 2016 data sets from the Niobrara River

Image date	November 8, 2012	August 15, 2016	August 18, 2016
Number of spectral bands	31	48	
Wavelength range (nm)	414.4–984.0	376.61–1,046.36	
Full-width half maximum (nm)	±9.5	±7.15	
Flying height above ground level (m)	1,228	1,023	
Pixel size (m)	0.6	0.5	
GCP RMSE [number of GCP] (m)[a]	2.20 [8]	0.67 [20]	2.22 [20]
Discharge (m^3/s)[b]	17.0	14.2	13.4
Turbidity (NTU)[c]	13.2	11.2	6.5

Note. CASI = Compact Airborne Spectrographic Imager; GCP = ground control point; NTU = nephelometric turbidity unit; RMSE = root mean square error.

[a]Ground control point root mean squared error is a metric of image georeferencing accuracy based on tarps surveyed in the field and visible in the images; see text for details.

[b]Mean daily discharge recorded at the nearest U.S. Geological Survey gaging station (#06461500), relative to mean annual discharge of 21 m^3/s (Alexander et al., 2009).

[c]Turbidity measurements were made directly in the field during each flight using a Eureka Manta-2 multiprobe in 2012 and a WetLabs EcoTriplet in 2016.

This procedure avoided the more complex process of transforming and resampling pixels that was required for the 2012 image. To evaluate georeferencing accuracy, we placed tarps in the field during each flight, two tarps in 2012 and five in 2016, and surveyed all four corners of each tarp. Comparing the coordinates of the tarps in the images to their field-surveyed locations resulted in the root mean square error values in Table 1, which were based on 8 ground control points in 2012 and 20 in 2016.

Images were subset to the spatial extent of the field data, and a binary mask was used to exclude non-water portions of the image. Channel masks were created using the longest wavelength band to identify a threshold that distinguished between water and terrestrial surfaces. Additional manual editing of masks was performed as needed. Finally, a Weiner spatial smoothing filter was applied within a 3 × 3 pixel moving window to reduce image noise.

2.2 | Field measurements of depth

To calibrate depth retrieval algorithms and evaluate their accuracy, *in situ* measurements of flow depth are necessary. During each image acquisition, we surveyed topography along a 1.5-km reach centred on a county road bridge near a bedrock knick point locally known as Norden Notch (Legleiter et al., 2017). Bed elevations were measured by establishing a local base station and wading the channel with real-time kinematic (RTK) GPS rovers. These RTK surveys consisted of systematic transects spaced approximately every 100 m, as well as points along the crests and bases of migrating sandbars (Figure 1 b). Water surface elevation (WSE) measurements were made along banks and where transects intersected islands. During 2016, we also used a SonTek River Surveyor S5 acoustic Doppler current profiler (ADCP) with the vertical beam as the primary depth reference (Mueller, Wagner, Rehmel, Oberg, & Rainville, 2013). The ADCP was mounted on a kayak, and the draft of the sensor below the water surface was measured carefully. We used the ADCP to survey deeper areas of the channel on along-stream profiles and thus supplement the lower density RTK wading measurements. For the August 15, 2016, image, RTK surveys were not conducted until several hours after image acquisition, so we only used ADCP data collected during image acquisition to avoid potential alignment errors resulting from bed deformation during this time period.

We used the RTK survey data to calculate water depth as the difference between water surface and bed elevations. For cross sections, an automated process was used to calculate depths by fitting a transect through each cross section and subtracting bed elevations from the mean of the nearest WSE pair (Legleiter et al., 2011).

To estimate WSE on bars, we transformed all WSE points from channel edges and islands to a channel-centred coordinate system with an s axis increasing in the downstream direction. Using the streamwise coordinates, we produced a surface relating WSE to streamwise distance, extracted WSE values at bar survey points, and calculated depths by subtracting bed elevations. For the 2016 data, the low density of WSE measurements recorded along the left bank at the downstream end of the reach resulted in an unrealistic WSE surface and negative depth estimates for some bars. For this reason, bar surveys were excluded from the 2016 field data set (Table 2).

Pixel-scale mean depths were calculated from the original survey points and randomly split into two subsets: one for calibrating depth retrieval algorithms and the other for assessing the accuracy of the resulting bathymetric maps. These data sets were produced by randomly assigning each field observation to either the calibration or validation subset, resulting in two equally sized data sets drawn from the same parent distribution of depths.

2.3 | Field spectroscopy and reflectance retrieval

On August 15 and 18, 2016, ground-based reflectance measurements were taken directly above the water surface using an analytical spectral devices FieldSpec3 spectroradiometer (Legleiter & Kinzel, 2017). Prior to data collection, the instrument was optimized using a 100% reflectance reference panel and reflectance spectra recorded relative to this standard. At each spectral measurement site, bed elevation was measured via RTK GPS and nearby WSE points used to calculate depth. On August 15 and 18, respectively, 38 and 42 field spectra were collected with depths ranging from 0.05 to 0.81 m.

Field spectra also were used to convert the 2016 images from radiance to reflectance by performing an empirical line calibration. This technique uses field spectra from calibration targets within the image to develop regression models that relate at-sensor radiance to surface reflectance. Our calibration spectra included a cement bridge and black, white, and blue tarps placed on riverbanks on August 15 and 18, 2016.

2.4 | Depth retrieval methods

Standard approaches to spectrally based bathymetric mapping require a relationship between depth d and some remotely sensed quantity X. We tested three previously published methods for establishing X versus d relations to evaluate which approach might be most effective for mapping the bathymetry of dynamic, sand-bed rivers such as the Niobrara. The first two techniques were variants of the optimal band ratio analysis (OBRA) framework introduced by Legleiter et al. (2009): one based on spectra extracted from the CASI images and the other using reflectance

TABLE 2 Summary of the number and type of field-based depth measurements associated with each of the hyperspectral images

	November 8, 2012	August 15, 2016	August 18, 2016
Total number of points	1,144	8,738	7,036
RTK cross-sections	895	0	240
RTK bar surveys	249	0	0
ADCP	0	8,738	6,796

Note. ADCP = acoustic Doppler current profiler; RTK = real-time kinematic.

spectra measured directly in the field. The third, more recent method is based on distributions of depths and image pixel values and is called image-to-depth quantile transformation, or IDQT (Legleiter, 2016).

2.4.1 | Method 1: OBRA of image data

A common way to define X is a ratio-based transformation of image pixel values:

$$X = \ln\left(\frac{R(\lambda_1)}{R(\lambda_2)}\right), \quad (1)$$

where R (λ) are reflectance values for spectral bands centred at wavelengths λ_1 and λ_2. This algorithm isolates the effect of depth on the total radiance signal and reduces the influence of other complicating factors such as the reflectance of the streambed (Dierssen, Zimmerman, Leathers, Downes, & Davis, 2003). The first method we evaluated involved calculating X by extracting image spectra at the locations of all surveyed depths in the calibration data set. The OBRA algorithm was used to identify the best combination of bands to define X for each image. OBRA regresses depth measurements d against X for all possible band ratios and identifies the optimal band ratio as that for which the resulting values of X explain the greatest amount of the variance in d and thus has the highest coefficient of determination R^2. The d versus X regression equation associated with the optimal band ratio is applied to each image pixel to produce a map of depth (Legleiter et al., 2009). As in previous applications of OBRA, we used linear and quadratic regressions but also considered an alternative local estimation, or lowess, model (Helsel & Hirsch, 2002) to improve the fit of the d versus X relationship. The term *lowess* is short for "locally weighted scatter plot smooth," as the method uses locally weighted linear regression with a linear polynomial to smooth data. We performed this analysis using the MATLAB function "smooth" with the "lowess" fit type and a span set to 20% of the total number of data points (Mathworks, 2017).

2.4.2 | Method 2: Calibration of OBRA using field spectra

The second method we tested involved using ground-based reflectance measurements, rather than image pixels, to define X (Equation 1) and calibrate an OBRA relation. Whereas these field spectra were essentially continuous, with a reflectance measurement every nanometre from 400 to 900 nm, the image data consist of a smaller number of discrete, broader spectral bands. To use a d versus X relation based on field spectra to predict depth from a CASI image, the optimal wavelengths identified by OBRA of the field spectra must correspond with specific image bands. To account for this issue, we used the matrix of R^2 values produced via OBRA of the field spectra to select a pair of wavelengths that coincided with a pair of discrete bands in the CASI image. As a criterion for selecting an appropriate pair of CASI image bands for the ratio, we ensured that the wavelengths of the two bands from the CASI image yielded an R^2 value as close as possible to that of the optimal pair of wavelengths identified via OBRA of the continuous field spectra. The d versus X regression coefficients associated with the selected band ratio were then applied throughout the reflectance image to estimate depth.

2.4.3 | Method 3: Image-to-depth quantile transformation

The third method we tested is a more recently introduced technique, known as IDQT, that was developed for use where simultaneous field measurements of depth from the time of image acquisition are not available, sparse, or of poor quality (i.e., not georeferenced). Unlike regression-based approaches that rely on pairing surveyed depths to specific image pixel values, IDQT predicts depth by linking the cumulative distribution function (CDF) of the image-derived quantity M to the CDF of depth d. M is defined by extracting pixel values from a single-band image, which can be obtained via various transformations of the original image data or by taking a band ratio. The CDF of d was defined using the same data sets used for OBRA, consisting of pixel-scale mean depths. For each pixel, M and d are scaled by their reach-averaged mean values $\langle M \rangle$ and $\langle d \rangle$, resulting in the normalized variables $M/\langle M \rangle$ and $d/\langle d \rangle$. The quantile transformation phase of IDQT determines the CDF probability of the $M/\langle M \rangle$ value of each pixel and then identifies the $d/\langle d \rangle$ value on the depth CDF that corresponds to this probability. These scaled variables can be used to produce a relative depth map ($d/\langle d \rangle$) that shows where depths are greater or less than the reach-averaged mean depth. An absolute bathymetric map can be obtained by multiplying $d/\langle d \rangle$ values for each pixel by $\langle d \rangle$ (Legleiter, 2016).

Depth retrieval via IDQT requires that the image-derived quantity M be monotonically related to depth. We tested two different approaches for defining M. First, we applied Lyzenga's (1978) deep-water correction to the images to isolate the bottom-reflected portion of the radiance signal. The resulting images were then processed using a minimum noise fraction (MNF) transformation (Green, Berman, Switzer, & Craig, 1988). We retained the first MNF band to define M because this band captured the largest amount of variability within the image data. The second approach to defining M involved selecting a band ratio image produced using Equation 1. We considered multiple band combinations and evaluated their correlation with depth by visually assessing whether spatial patterns of image brightness were consistent with our field observations of channel morphology. We intentionally did not define M by using OBRA to identify the optimal band ratio because reliance on OBRA would diminish IDQT's primary advantage of not requiring survey data concurrent with image acquisition.

2.5 | Accuracy assessment and method comparison

For all three calibration methods, depth retrieval errors were calculated using the validation subset of the field-surveyed depths as

$$\varepsilon(j) = d_f(j) - d_i(j), \quad (2)$$

where $\varepsilon(j)$ is the error at location j, $d_f(j)$ is the pixel-scale mean depth, and $d_i(j)$ is the depth predicted for the corresponding image pixel. For each method and image date, we computed the mean, median, and standard deviation of the depth retrieval errors. The mean and median errors provided an indication of bias: systematic overprediction or underprediction of depth from an image. The standard deviation of the errors quantified depth retrieval precision. Error maps also allowed us to examine the spatial distribution of errors throughout the reach.

Algorithm performance also was evaluated by performing observed versus predicted (OP) regressions between field-surveyed depths (d_f) and image-derived estimates (d_i; Piñeiro, Perelman, Guerschman, & Paruelo, 2008). If the depth retrieval algorithm perfectly predicted depth, this regression would result in an intercept of 0 and slope of 1. OP regression coefficients and R^2 values indicate how far depth predictions deviate from the 1:1 line of perfect agreement.

3 | RESULTS

Using hyperspectral images of the Niobrara, we evaluated three depth retrieval techniques in a sandy, dynamic river environment. We applied each method to all three CASI images except for the field spectra-based calibration because no ground-based reflectance data were collected in 2012. Below, we assess the accuracy of each algorithm separately.

3.1 | Method 1: OBRA of image data

For the first method, OBRA of image data, we also considered a local estimation model as an alternative to standard regression.

3.1.1 | Regression-based OBRA

Although we performed OBRA using both linear and quadratic formulations, in all cases, the quadratic version with an X^2 term produced the highest R^2 values, and we thus focus on quadratic OBRA. The results of this analysis are summarized in Figure 2, with the optimal band ratio for each image yielding R^2 values of 0.81, 0.81, and 0.83. The matrices of R^2 values shown in Figure 2 represent how much of the variability in d is explained by X. For all three images, strong correlations occur in the upper left region of the R^2 matrices, where a numerator band in the blue-green portion of the spectrum ($450 < \lambda_1 < 600$ nm) is paired with a red denominator band ($600 < \lambda_2 < 710$ nm). This broad region of high R^2 values suggests that several other band ratios would have yielded d versus X relationships nearly as strong as the optimal combination.

Accuracy assessment of the OBRA-based bathymetric maps confirmed this technique's ability to retrieve depth on the Niobrara River. OP regression R^2 values were high, ranging from 0.81 to 0.83 and averaging 0.817 (Table 3). The slope and intercept of these regression equations were also near 1 and 0, respectively, indicating that OBRA-based depth estimates generally were unbiased. For all three images, mean and median depth retrieval errors were <1 cm. These small error

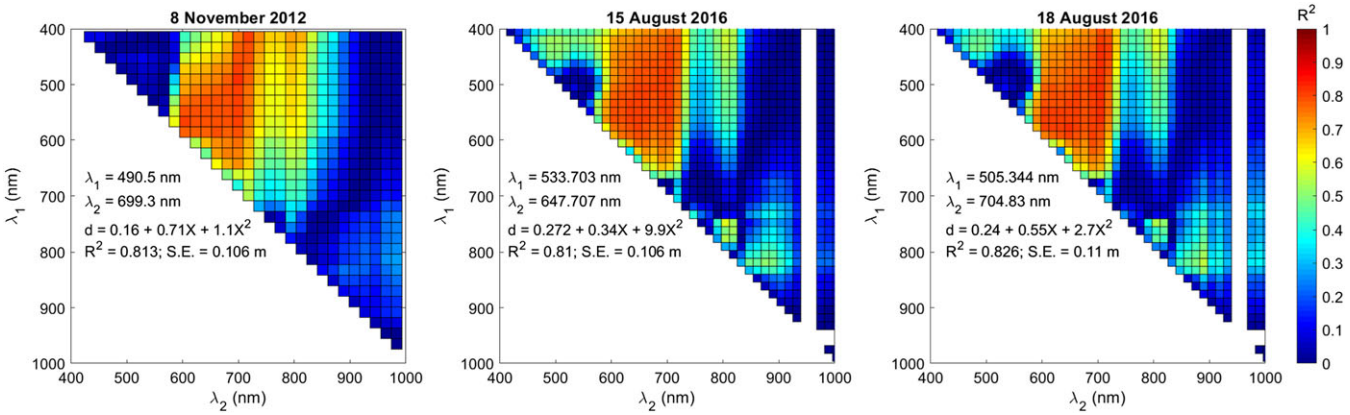

FIGURE 2 Results of optimal band ratio analysis for all three images [Colour figure can be viewed at wileyonlinelibrary.com]

TABLE 3 Summary of accuracy assessment for all three depth retrieval techniques

	OBRA of image data	OBRA based on field spectra	IDQT
Minimum predicted depth (m)	−0.121	−2.600	0
Maximum predicted depth (m)	2.681	7.555	1.697
Minimum error (m)	−0.595	−0.290	−0.839
Maximum error (m)	0.596	1.068	0.527
Mean error (m)	−0.005	0.068	−0.204
Median error (m)	0.003	0.104	−0.209
Standard deviation of error (m)	0.104	0.155	0.133
First quartile of error (m)	−0.051	0.006	−0.270
Third quartile of error (m)	0.051	0.157	0.120
OP R^2	0.817	0.725	0.753
OP slope	0.992	1.6	0.824
OP intercept	0.006	−0.156	−0.101

Note. For regression-based OBRA of image data and IDQT, values from the three images analysed were averaged. OBRA based on field spectra was only evaluated for the two images acquired in 2016 because no field spectra were collected in 2012; the results for this method thus are averages for the two 2016 images. For OBRA of image data, the results reported in this table are for standard regression models, but local estimation models produced very similar results.

IDQT = image-to-depth quantile transformation; OBRA = optimal band ratio analysis; OP = observed versus predicted.

values suggest that even in turbid, dynamic channels, a simple *d* versus *X* relationship can yield accurate, unbiased depth information when field measurements of depth concurrent with image acquisition are available for calibration.

The spatial distribution of depth retrieval errors can be visualized by mapping prediction errors on the CASI images (Figure 3). For all three images, large errors often occurred along channel edges. For the November 8, 2012, image, large errors also occurred at bar survey points. Figure 3 shows depth retrieval errors for the 2012 image and illustrates the concentration of the largest errors at both bar crests and channel margins. Despite low mean errors, OBRA did not capture the full range of depths present within the channel. For all three images, the minimum OBRA-predicted depth was on average 0.11 m larger than the minimum depth surveyed in the field. This result implies that the quadratic *d* versus *X* relation overpredicts depth for the shallowest areas of the channel.

3.1.2 | Local estimation-based OBRA

As an alternative to the quadratic regression between *X* and *d*, we used a local estimation, or lowess, model to fit the *d* versus *X* relationship with the goal of improving the range of OBRA-based depth predictions. Differences between the quadratic and lowess fits for the August 18, 2016, image are illustrated in Figure 4. The most notable difference between the models is that the slope of the quadratic function changes from positive to negative towards the lower limit of *X*, erroneously implying an increase in depth for the smallest *X* values and resulting in minimum predicted depths that are greater than the shallowest depths observed in the field. In contrast, the lowess model accurately depicts a direct relationship between *X* and *d* over the entire range of *X*. This difference is manifested by the minimum depth predicted by the lowess and quadratic models. For the August 18, 2016, image, the minimum depth predicted by lowess (0.13 m) is closer to the minimum surveyed depth (0.008 m) than that of the quadratic fit (0.21 m), suggesting that lowess-based OBRA could predict shallow depths with greater accuracy than quadratic OBRA. Despite improvement to the range of depths predicted by OBRA, the overall accuracy of lowess-based OBRA was similar to quadratic OBRA. Values of R^2 for the lowess and quadratic *d* versus *X* regression relations were both 0.83, and the error statistics and OP regressions for lowess were very similar to standard OBRA (Table 4). Because the lowess fit did not yield significantly greater depth retrieval accuracy, we used the results from standard quadratic OBRA for comparison with the other depth retrieval methods we evaluated.

3.2 | Method 2: OBRA based on field spectra

To estimate depths from the 2016 images using a relationship based on field spectroscopy, we defined *X* using ground-based reflectance measurements as input to OBRA. R^2 values resulting from the *d* versus *X* regression of every possible combination of wavelengths (λ_1, λ_2) are illustrated in Figure 5 for the August 15 and 18 data sets. For the field spectra, linear regression performed just as well as the more complex quadratic formulation of OBRA, with the optimal band pair yielding R^2 values of 0.98 and 0.88 for the two dates. These findings confirmed a strong relationship between depth and reflectance and implied that depth could be predicted from hyperspectral images calibrated to units of surface reflectance.

As described in Section 2.4.2, the optimal wavelengths identified by OBRA of the continuous field spectra did not necessarily correspond with a specific pair of CASI image bands, so we chose an alternative band ratio that matched the centre wavelengths of two particular bands in the image. The field spectroscopy-based OBRA matrices demonstrated that a wide range of wavelength combinations was strongly related to depth, so selecting a pair of wavelengths that matched specific CASI band centres was not difficult. The alternative band ratios selected for the August 15 and 18 images were 562/705 and 577/605 nm, respectively.

Overall, field spectroscopy-based OBRA exhibited a slight shallow bias and was less accurate than image-based OBRA, with mean

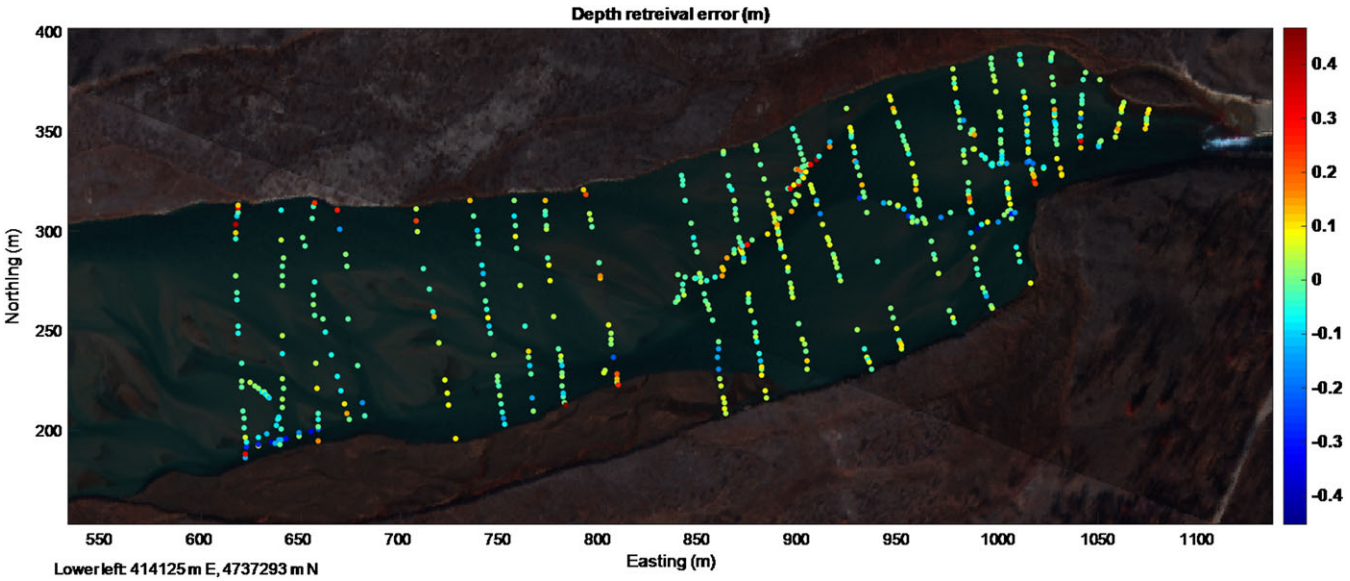

FIGURE 3 Depth retrieval error map for optimal band ratio analysis-based bathymetric map produced from the November 8, 2012 image. Error values were calculated using Equation 2 [Colour figure can be viewed at wileyonlinelibrary.com]

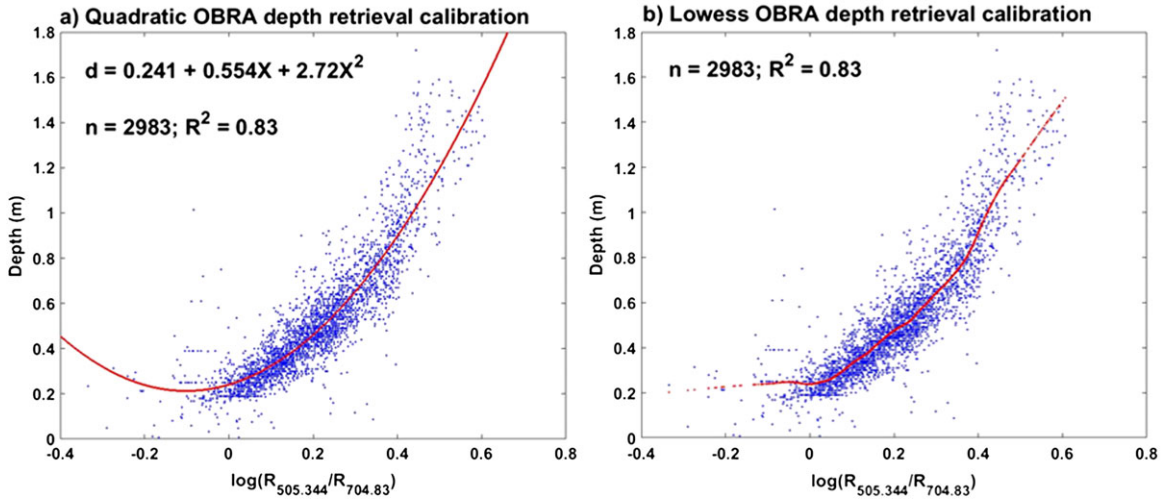

FIGURE 4 Calibration of the *X* versus *d* relationship using a (a) quadratic and (b) local estimation (lowess) model for the August 18, 2016, data set. OBRA = optimal band ratio analysis [Colour figure can be viewed at wileyonlinelibrary.com]

TABLE 4 Comparison of depth retrieval errors and OP regression statistics for optimal band ratio analysis of the August 18, 2016, image based on standard quadratic regression and a lowess fit

	Quadratic	Lowess
Mean error (m)	−0.0003	0.0020
Minimum error (m)	−0.6299	−0.6181
Maximum error (m)	0.7080	0.6821
Median error (m)	−0.0077	−0.0089
Standard deviation of error (m)	0.1117	0.1096
First quartile of error (m)	−0.0597	−0.0586
Third quartile of error (m)	0.0487	0.0466
OP R^2	0.83	0.83
OP slope	1	1
OP intercept	−0.0012	−0.0022

Note. OP = observed versus predicted.

(median) error values of 0.068 (0.026) and 0.14 (0.11) m for the August 15 and 18 images, respectively. OP regressions had R^2 values of 0.71 and 0.74, respectively; however, OP regression slopes >1 and intercepts <0 indicated a systematic depth retrieval bias. This bias is further confirmed by a difference between the range of depths predicted and those observed in the channel. Both the August 15 and 18 depth maps did not capture the deepest areas of the channel. The depth maps also contained large negative estimates that lead to large positive error values. These erroneous depth predictions occurred mainly in small, concentrated areas, but most of the field spectra-based bathymetric maps provided realistic representations of depth.

3.3 | Method 3: Image-to-depth quantile transformation

3.3.1 | Comparing IDQT of different *M* inputs

IDQT involves linking the CDF's of an image-derived variable *M* and field-surveyed depth *d*. The critical assumption made in this process is that *M* is monotonically related to *d*. We tested the strength of the relationship between *M* and *d* for two different ways of defining *M*. Because IDQT is designed to avoid having to pair field-surveyed depths with specific pixels, we only used the field-surveyed depths to quantify the strength of the agreement between *d* and the various candidates for defining *M*. In practice, the strength of *d* versus *M* relations could be based on a qualitative visual inspection of potential *M* images. Using the Lyzenga and MNF transforms to define *M* resulted in R^2 values of 0.47 and 0.57 for the 2016 images and 0.73 for the 2012 image. This poor correlation, particularly for the 2016 images, motivated us to assess an alternative approach: defining *M* as a band ratio image produced via Equation 1. For each image date, we examined multiple band ratio combinations before selecting one that appeared to correspond most closely with patterns of depth. Table 5 summarizes all the tested band ratio combinations for each image and their resulting correlation with depth. For the two images acquired in 2016, defining *M* using band ratios rather than MNF band 1 improved the R^2 values of the *M* versus *d* regressions to 0.73–0.78. We thus used band ratios to define *M* for those two images: 477/662 and 490/719 nm for the August 15 and 18 images, respectively. We used MNF band 1 to define *M* for the 2012 image because its correlation with depth was reasonably strong, with an R^2 value of 0.73, nearly as high as the band ratios we considered (Table 5).

3.3.2 | Depth retrieval by IDQT

OP regressions for IDQT-based bathymetric maps yielded R^2 values ranging from 0.70 to 0.79. The slopes of these OP regression equations were <1 for all images, and intercepts were <0 for the 2016 images, implying that depths predicted via IDQT were biased deep. All three images had negative mean errors that indicated overprediction of depth via IDQT. The strongest deep bias was observed for the August 2016 images, both having mean and median error values <−0.20 m. This bias was less apparent for the November 2012 image, with a mean (median) error of −0.099 (−0.087) m.

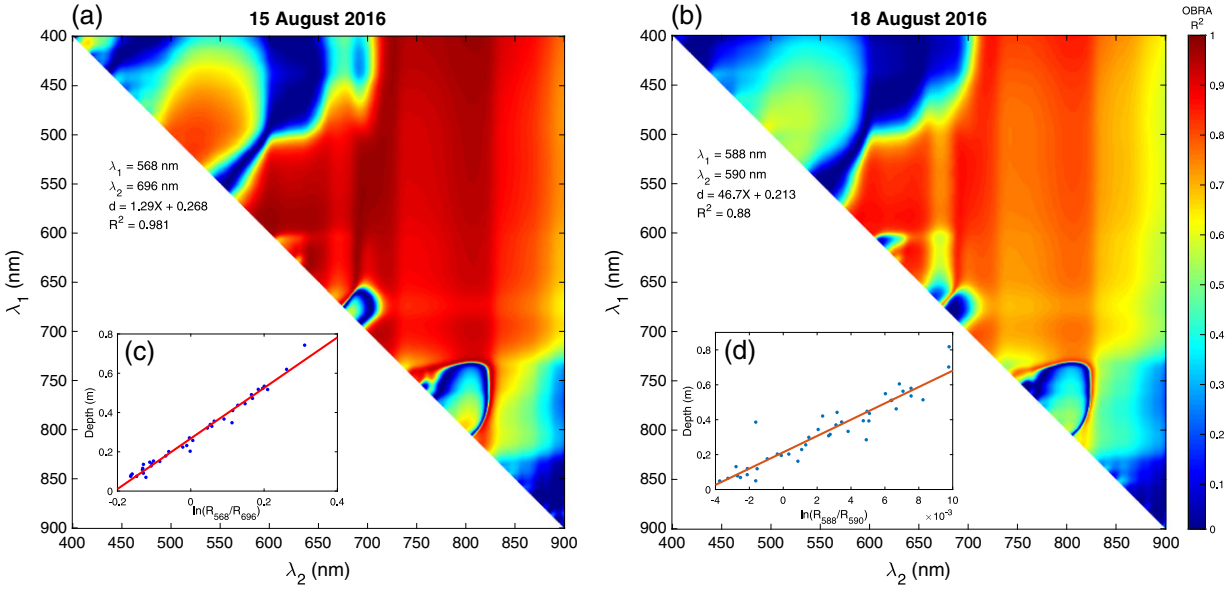

FIGURE 5 Optimal band ratio analysis of field spectra collected on August 15 and 18, 2016. (a and b) These R^2 matrices summarize the strength of the relationship between *X* and *d*. (c and d) Calibration plot of *X*, defined using the optimal band ratio, and field-surveyed depth [Colour figure can be viewed at wileyonlinelibrary.com]

TABLE 5 Band ratio combinations tested in defining the log-band ratio *M* image for IDQT analysis and R^2 values yielded from corresponding *d* versus *M* regression

	Numerator band λ_1 (nm)	Denominator band λ_2 (nm)	R^2
November 8, 2012	547.50	661.40	0.77
	528.50	699.30	0.77
	547.50	756.30	0.71
August 15, 2016	476.63	661.95	0.78[a]
	533.70	718.90	0.72
	505.17	647.71	0.78
August 18, 2016	490.91	718.90	0.73[a]
	547.96	733.13	0.6
	505.17	690.42	0.73

Note. For the 2012 image, we used minimum noise fraction band 1, which yielded an R^2 value just as high as any of the band ratio images.

IDQT = image-to-depth quantile transformation.

[a]The band ratio ultimately selected to define *M* for IDQT.

4 | DISCUSSION

Most prior studies evaluating the ability to infer depth from passive optical images have focused on clear-flowing, gravel-bedded rivers (Marcus & Fonstad, 2008). In contrast to these favourable conditions, the reduced water clarity and high mobility of sand-bedded channels make spectrally based bathymetric mapping not only more difficult (Legleiter et al., 2011) but also more important because the mobile-bed conditions all but preclude capturing a "frozen," instantaneous spatial snapshot of the bed topography via conventional field surveys. The purpose of this study was to assess the performance of different depth retrieval methods developed on clear-flowing rivers for predicting depth in more turbid and dynamic sand-bed rivers. Each of the three bathymetric mapping methods we considered demonstrated potential to provide useful depth information from sandy, live-bed channels. However, each method also was subject to certain limitations. When selecting the best method for remote sensing of sand-bed rivers, one must consider the available data, project budget, and intended use of the bathymetric maps. Below, we compare the performance of the three techniques and summarize the advantages and drawbacks of the algorithms individually.

4.1 | Algorithm comparison

A summary of depth retrieval error statistics, OP regressions, and range of depths predicted by bathymetric maps is shown for each method in Table 3.

Summary values were calculated by averaging individual statistics across the three image dates. On average, OBRA of image data using quadratic regression provided the most accurate depth predictions, with a mean error value closest to zero (−0.005 m) and the smallest range of depth retrieval errors. In comparison, IDQT had a systematic deep bias, and field spectra-based OBRA had a shallow bias, with mean error values of −0.204 and 0.068 m, respectively. Despite these differences in mean error, the standard deviations of error for each method were similar, ranging from 0.104 to 0.155 m, implying that the precision of the three methods was comparable.

An important advantage of IDQT over regression-based calibration methods was the absence of negative depth estimates. Because depth predictions obtained via IDQT are bounded by the input CDF of depths, in our case based on surveyed depths, IDQT more effectively captures the full range of depths present in the channel. However, these advantages are countered by the deep bias of IDQT-based bathymetric maps. Among all three methods, IDQT had the largest negative mean and median depth retrieval errors (−0.204 and −0.209 m). Figure 6a shows a side-by-side comparison of IDQT and OBRA-based bathymetric maps and resulting errors for the August 18, 2016, image and illustrates differences between the two methods. For example, the more extensive dark blue tones in the IDQT-based

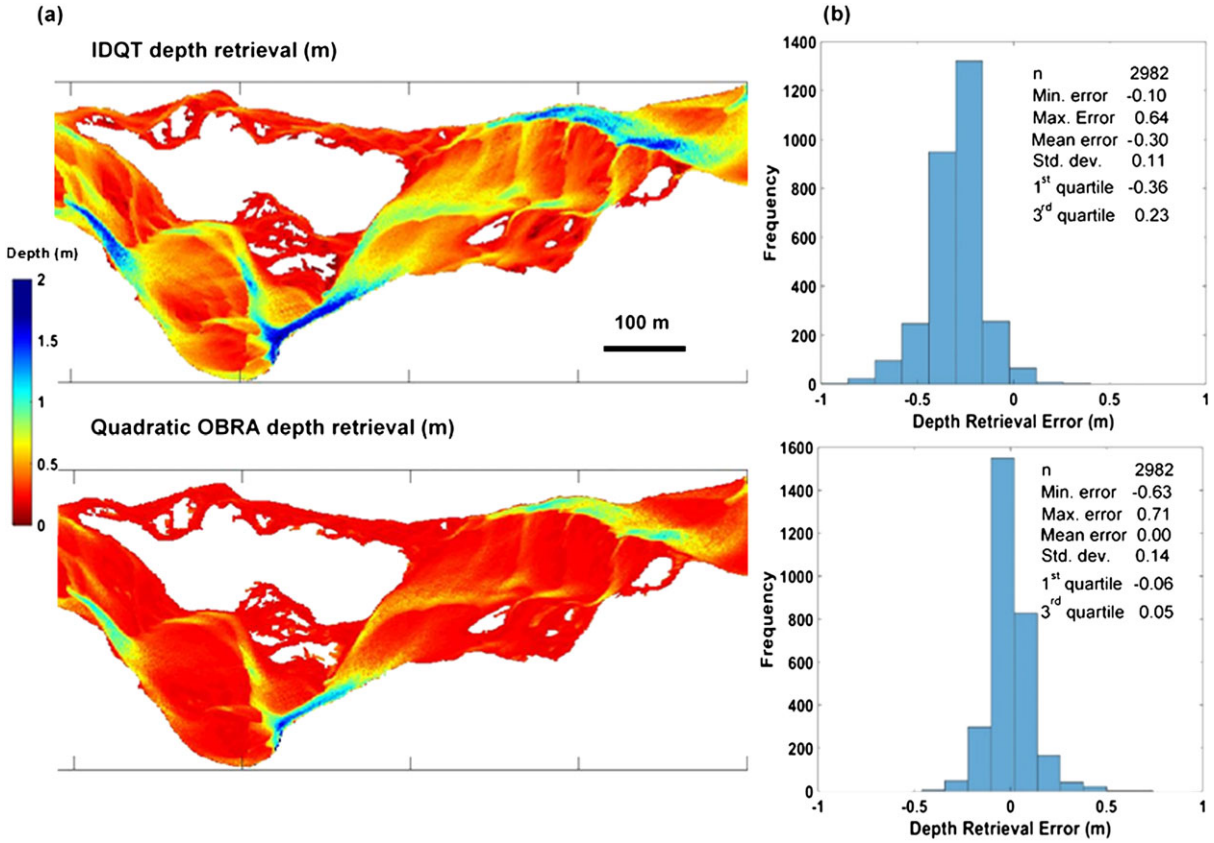

FIGURE 6 (a) Comparison of image-to-depth quantile transformation (IDQT)-based bathymetric map (top) and optimal band ratio analysis (OBRA)-based bathymetric map (bottom) for the August 18, 2016, Compact Airborne Spectrographic Imager image. Maps share a common colour scale bar. (b) Histograms of depth retrieval errors and summary statistics for each bathymetric map [Colour figure can be viewed at wileyonlinelibrary.com]

map indicated overpredictions of depth, but this map also more effectively captures shallow margins than the OBRA-based map, which lacks dark maroon colours representing depths near zero. The more negative first quartile of error for IDQT (−0.36 m) versus OBRA (−0.06) also confirms the greater deep bias of the IDQT-based bathymetric map (Figure 6b).

4.2 | Quadratic regression- and local estimation-based OBRA

The original development and testing of OBRA occurred on clear-flowing, gravel-bedded rivers (Legleiter et al., 2009). Given the more turbid, complex, and dynamic nature of the Niobrara River, the accuracy of OBRA could be limited in this type of river environment. Specifically, because OBRA relies upon exact alignment of ground-based depth measurements and the corresponding image pixels, migration of bed forms in the time between field surveys and image acquisition could interfere with the pairing of remotely sensed and field-measured quantities. The initial image georeferencing errors detailed in Section 2.1.1 and summarized in Table 1 suggested misalignment between field and image data might have limited the accuracy of depth retrieval via OBRA for our data set. Despite these obstacles, OBRA yielded the smallest overall depth retrieval error of the three methods and therefore offered the most reliable means of bathymetric mapping on the Niobrara. Although the mean and median error values for OBRA were near 0 m, the quadratic formulation of OBRA resulted in negative depth estimates and overprediction of depth in the shallowest areas of the channel. Given that these shallows provide critical aquatic habitat for local fish species (Peters & Holland, 1992) and foraging habitat for federally listed bird species (Le Fer, Fraser, & Kruse, 2008), accurate depth retrieval in these regions is important. Using a local estimation (lowess) model in place of the quadratic regression provided a more realistic fit in that d increased with X over the entire range of X values.

The concentration of large depth retrieval errors along channel margins for OBRA-based bathymetric maps could be explained in part by the existence of mixed pixels containing both water and surrounding terrestrial land cover. The inclusion of non-water surfaces in such pixels would cause the d versus X relation to fail. Additionally, lingering misalignment issues between field and image data would be most problematic at channel margins where in-channel survey points could fall outside of the channel as represented in the image. These alignment issues were also apparent in the large error values along bar faces. Where depth is changing rapidly, such as the steep slope of bar faces, achieving co-registration of image pixels and depth survey points is more difficult. Additionally, pixels in areas with steep bed slopes could encompass a range of depths, such that any misalignment could result in a large change in d (and X) and thus create another source of error for OBRA.

Although most of the Niobrara consists of shallow water <1.5 m, saturation of the radiance signal in deeper water is a general problem

encountered in the remote sensing of rivers. Before applying OBRA, one must also consider the potential for the *d* versus *X* relationship to saturate in deep areas of sediment-laden channels. Perhaps the largest drawback of OBRA is the requirement of an extensive in-channel topographic survey during image acquisition. The field work required to survey the channel is laborious and expensive and might not be a realistic option for many projects. Moreover, the necessity of ground-based data undermines one of the main attractions of remotely sensed bathymetric mapping: the ability to reduce, if not eliminate, field data collection. An important topic for further research is evaluating the number, density, and spatial configuration of ground-based depth measurements required to establish an OBRA relationship. If reasonably accurate depth predictions can be obtained based on only a small field data set, OBRA could have significant value as a "survey multiplier."

4.3 | Field spectra-based OBRA

If *in situ* depth measurements cannot be obtained concurrently with image acquisition and the bed is highly mobile, field spectroscopy could offer a simpler, less fieldwork-intensive option. Depths can be measured directly at the same time the field spectra are recorded, and these coupled observations of depth and reflectance used to calibrate a general *d* versus *X* relation that could then be applied to a reflectance image. Although the overall accuracy of the field spectra-based depth retrieval was inferior to image-based OBRA, the field spectra-based depth maps were spatially coherent. In some areas, large negative and unrealistically large depths were predicted, but these errors were not extensive and potentially could be reduced by implementing a more rigorous atmospheric correction approach. In this study, we used an empirical line calibration to convert the hyperspectral images to units of surface reflectance because this method is relatively simple and computationally efficient. However, a more complex radiative transfer model might have provided more accurate reflectance images and hence depth estimates. Because the reflectance images were not used in the image-based OBRA and IDQT analyses, these methods had the advantage of not being subject to the potential error introduced by atmospheric correction.

4.4 | Image-to-depth quantile transform

IDQT offers an alternative strategy to standard regression-based approaches to depth retrieval that rely upon pairing field observations and pixel values. In contrast to OBRA, IDQT avoids negative depth estimates and is insensitive to misalignment errors between image and field data (Legleiter, 2016). Given the difficulty of conducting topographic surveys and achieving precise georeferencing in dynamic channels such as the Niobrara, IDQT has the potential to facilitate depth retrieval in such environments. However, our results indicated that IDQT also will face some challenges. Among all three CASI images, IDQT overpredicted depth by >0.20 m. Because of this deep bias, a more useful IDQT output might be a relative depth map ($d/\langle d \rangle$), where absolute depth values *d* are scaled by the reach-averaged depth $\langle d \rangle$. By showing the general pattern of deep and shallow areas of the channel, this relative depth map might be useful for some river management applications where knowledge of absolute depth is not critical. For example, relative depth maps could be used to identify broad habitat units, as well as bar forms in the context of sediment transport studies.

One explanation for the deep bias of IDQT is that the field survey used to characterize the probability distribution of depth did not adequately represent all depths present within the channel. Ideally, ground-based depth surveys would maximize channel coverage and fully sample the channel morphology in an unbiased manner. In this study, the large proportion of ADCP data included in the 2016 depth data sets could have led to over-representation of deep regions in the depth CDF since ADCP data collection concentrated on deeper areas that were inaccessible by wading. These findings highlight the sensitivity of IDQT to the field sampling strategy and to fully realize the value of IDQT in sand-bedded rivers. Similarly, over-representation of deeper areas might have affected the results of image-based OBRA, which would depend to some degree on the distribution of depths used to calibrate *d* versus *X* regressions. Further investigation and testing of an unbiased means of quantifying the channel's depth distribution thus is needed.

5 | CONCLUSION

This study showed that multiple methods of depth retrieval from passive optical image data can provide reliable bathymetric information for sediment-laden, dynamic channels. Although the standard, image-based *d* versus *X* calibration approach via OBRA yielded the most accurate depth predictions, this method comes with some constraints that are particularly apparent in dynamic, sandy channels such as the Niobrara. Exact alignment of field and image data and simultaneous collection of field and image data are prerequisites to OBRA that are not necessary for such approaches as IDQT and field spectroscopy-based calibration. Using field spectra to define the radiometric quantity *X* in defining an OBRA relationship produced bathymetric maps that were less accurate than traditional OBRA but still spatially coherent. Although IDQT exhibited a strong deep bias in this study, IDQT-produced depth maps still provided information on the general distribution of depth. The potential for IDQT to improve the practicality of remotely sensing river bathymetry highlights the need for additional testing and refinement of this technique, especially characterization of the distribution of depths within the channel.

ACKNOWLEDGEMENTS

Any use of trade, firm, or product names is for descriptive purposes only and does not imply endorsement by the U.S. Government. This investigation was supported by a grant from the Office of Naval Research Littoral Geosciences and Optics Program (N000141010873) and graduate student research grants from the Geological Society of America. Paul Kinzel, Robert Mahon, Marissa Murr, and Suleyman Naqshband assisted with field data collection. Access to the study area was graciously provided by The Nature Conservancy. Ed Bulliner and two anonymous reviewers provided useful comments.

ORCID

E. Dilbone http://orcid.org/0000-0001-7360-4057
C.J. Legleiter http://orcid.org/0000-0003-0940-8013
J.S. Alexander http://orcid.org/0000-0002-1602-482X
B. McElroy http://orcid.org/0000-0002-9683-4282

REFERENCES

Alexander, J. S., Zelt, R. B., & Schaepe, N. J. (2009). Geomorphic segmentation, hydraulic geometry, and hydraulic microhabitats of the Niobrara River, Nebraska—Methods and initial results. U. S. Geological Survey Scientific Investigations Report, 2009–5008, 51 p.

Alexander, J. S., Zelt, R. B., & Schaepe, N. J. (2010). Hydrogeomorphic and hydraulic habitats of the Niobrara River, Nebraska—With special emphasis on the Niobrara National Scenic River. U.S. Geological Survey Scientific Investigations Report, 2010–5141, 62 p.

Carbonneau, P., Fonstad, M. A., Marcus, W. A., & Dugdale, S. J. (2011). Making riverscapes real. *Geomorphology*, *137*(1), 74–86.

Dierssen, H. M., Zimmerman, R. C., Leathers, R. A., Downes, T. V., & Davis, C. O. (2003). Ocean color remote sensing of seagrass and bathymetry in the Bahamas Banks by high resolution airborne imagery. *Limnology and Oceanography*, *48*(1), 444–455.

Fuller, I. C., & Basher, L. R. (2013). Riverbed digital elevation models as a tool for holistic river management: Motueka River, Nelson, New Zealand. *River Research and Applications*, *29*(5), 619–633. https://doi.org/10.1002/rra.2555

Gaeuman, D. A., Schmidt, J. C., & Wilcock, P. R. (2003). Evaluation of in-channel gravel storage with morphology-based gravel budgets developed from planimetric data. *Journal of Geophysical Research – Earth Surface*, *108*. https://doi.org/10.1029/2002JF000002

Green, A. A., Berman, M., Switzer, P., & Craig, M. D. (1988). A transformation for ordering multispectral data in terms of image quality with implications for noise removal. *IEEE Transactions on Geoscience and Remote Sensing*, *26*(1), 65–74.

Helsel, D. R., & Hirsch, R. M. (2002). Statistical methods. In *U.S. Geological Survey techniques of water-resources investigations*, *Book 4*, *Chapter A3* (p. 522).

Johnsgard, P. A. (2007). *The Niobrara—A river running through time*. Lincoln, NE: University of Nebraska Press.

Lane, S. N., Westaway, R. M., & Hicks, D. M. (2003). Estimation of erosion and deposition volumes in a large, gravel-bed, braided river using synoptic remote sensing. *Earth Surface Processes and Landforms*, *28*(3), 249–271.

Le Fer, D., Fraser, J. D., & Kruse, C. D. (2008). Piping plover foraging-site selection on the Missouri River. *Waterbirds*, *31*(4), 587–592.

Legleiter, C. J. (2016). Inferring river bathymetry via image-to-depth quantile transformation (IDQT). *Water Resources Research*, *52*(5), 3722–3741.

Legleiter, C.J. (2017). Hyperspectral image data from the Niobrara River, Nebraska, November 2012 and August 2016: U.S. Geological Survey data release, https://doi.org/10.5066/F75M647F.

Legleiter, C. J. & Kinzel, P. J. (2017). Field spectra from the Niobrara River, Nebraska, August 15–18, 2016: U.S. Geological Survey data release, https://doi.org/10.5066/F7B856NC.

Legleiter, C. J., Kinzel, P. J., Alexander, J. A., & Dilbone, E. (2017). Field-based bathymetric surveys of the Niobrara River, Nebraska, November 2012 and August 2016: U.S. Geological Survey data release, https://doi.org/10.5066/F7NK3CJ7.

Legleiter, C. J., Kinzel, P. J., & Overstreet, B. T. (2011). Evaluating the potential for remote bathymetric mapping of a turbid, sand-bed river: 1. Field spectroscopy and radiative transfer modeling. *Water Resources Research*, *47*(9), W09531

Legleiter, C. J., Roberts, D. A., & Lawrence, R. L. (2009). Spectrally based remote sensing of river bathymetry. *Earth Surface Processes and Landforms*, *34*(8), 1039–1059.

Lejot, J., Delacourt, C., Piegay, H., Fournier, T., Tremelo, M.-L., & Allemand, P. (2007). Very high spatial resolution imagery for channel bathymetry and topography from an unmanned mapping controlled platform. *Earth Surface Processes and Landforms*, *32*(11), 1705–1725.

Lyzenga, D. R. (1978). Passive remote sensing techniques for mapping water depth and bottom features. *Applied Optics*, *17*(3), 379–383.

Marcus, A. W., & Fonstad, M. A. (2008). Optical remote mapping of rivers at sub meter resolutions and watershed extents. *Earth Surface Processes and Landforms*, *33*(1), 4–24.

Marcus, W. A., Legleiter, C. J., Aspinall, R. J., Boardman, J. W., & Crabtree, R. L. (2003). High spatial resolution hyperspectral mapping of in-stream habitats, depths, and woody debris in mountain streams. *Geomorphology*, *55*(1–4), 363–380. https://doi.org/10.1016/S0169%E2%80%93555X(03)00150%E2%80%938

Mathworks. (2017). Local regression smoothing. https://www.mathworks.com/help/curvefit/smoothing-data.html#bq_6ys3-3, accessed 8 December 2017.

McKean, J. A., Isaak, D. J., & Wright, C. W. (2008). Geomorphic controls on salmon nesting patterns described by a new, narrow-beam terrestrial-aquatic LiDAR. *Frontiers in Ecology and the Environment*, *6*(3), 125–130. https://doi.org/10.1890/070109

Mueller, D. S., Wagner, C. R., Rehmel, M. S., Oberg, K. A, & Rainville, Francois. (2013). Measuring discharge with acoustic Doppler current profilers from a moving boat (ver. 2.0, December 2013). *U.S. Geological Survey techniques and methods*, *Book 3*, *Chapter A22*, 95 p.

Peters, E. J., & Holland, R. S. (1992). Shallow-water fish community abundance and habitat use in the lower Platte River, Nebraska. University of Nebraska-Lincoln, Department of Forestry, Fisheries and Wildlife, Journal Series, No. 9109.

Piñeiro, G., Perelman, S., Guerschman, J. P., & Paruelo, J. M. (2008). How to evaluate models: Observed vs. predicted or predicted vs. observed? *Ecological Modeling*, *216*(3–4), 316–322.

Schaepe, N.J., Alexander, J.S., & Folz-Donahue, K. (2016). Effects of streamflows on stream-channel morphology in the eastern Niobrara National Scenic River, Nebraska, 1988–2010. *U.S.* Geological Survey Scientific Investigations Report 2016–5004, 30 p., https://doi.org/10.3133/sir20165004.

Tamminga, A., Hugenholtz, C. H., Eaton, B. C., & Lapointe, M. (2014). Hyperspatial remote sensing of channel reach morphology and hydraulic fish habitat using an unmanned aerial vehicle (UAV): A first assessment in the context of river research and management. *River Research and Applications*, *31*(3), 379–391.

Whited, D. C., Kimball, J. S., Lorang, M. S., & Stanford, J. A. (2013). Estimation of juvenile salmon habitat in Pacific Rim rivers using multiscalar remote sensing and geospatial analysis. *River Research and Applications*, *29*(2), 135–148.

Winterbottom, S. J., & Gilvear, D. J. (1997). Quantification of channel bed morphology in gravel-bed rivers using airborne multispectral imagery and aerial photography. *Regulated Rivers: Research & Management*, *13*(6), 489–499.

How to cite this article: Dilbone E, Legleiter CJ, Alexander JS, McElroy B. Spectrally based bathymetric mapping of a dynamic, sand-bedded channel: Niobrara River, Nebraska, USA. *River Res Applic*. 2018;34:430–441. https://doi.org/10.1002/rra.3270